

1 **Moisture transport dynamics in wood during drying studied by long-wave near-infrared**  
2 **hyperspectral imaging**

3 -----

4

5 **Te Ma<sup>1</sup>, Genki Morita<sup>1</sup>, Tetsuya Inagaki, and Satoru Tsuchikawa\***

6 Graduate School of Bioagricultural Sciences, Nagoya University, Furo-Cho, Chikusa, Nagoya

7 464-8601, Japan, Email address: st3842@agr.nagoya-u.ac.jp

8 \*Corresponding author: Satoru Tsuchikawa

9

10 **<sup>1</sup> The first two authors, Te Ma and Genki Morita contributed equally to this study (co-**  
11 **first author)**

12

13 Funding: This study is supported by JSPS (KAKENHI, no.19K15886)

14 Conflicts of interest/Competing interests: Not applicable

15 Availability of data and material: Yes

16 Code availability: Not applicable

17 Authors' contributions:

18 Te Ma: Methodology, Data curation, Validation, Writing-Original draft preparation

19 Genki Morita: Methodology, Data curation, Validation, Writing- reviewing and editing

20 Tetsuya Inagaki: Methodology, Conceptualization, Writing- reviewing and editing

21 Satoru Tsuchikawa\*: Supervision, Conceptualization, Writing- reviewing and editing

22 Ethics approval: Not applicable

23 Consent to participate: Not applicable

24 Consent for publication: Not applicable

25

26 **Abstract:**

27 The complexities of wood microstructure cause difficulties in understanding water movement  
28 characteristics during drying. Here, the water transport dynamics in softwood (Japanese cypress) with  
29 different sample lengths (30 mm, 60 mm, and 90 mm) and various drying temperatures (30°C, 60°C,  
30 and 90°C) were studied using a rapid and high-resolution moisture content (MC) mapping method based  
31 on long-wave near-infrared hyperspectral imaging (NIR-HSI). The observations of this study are as  
32 follows: slow drying at approximately 30°C, the area near the subsurface of the wood samples tends to  
33 have higher MC than the central parts during drying, especially in the case of longer wood samples. For  
34 drying at higher temperatures, strongly bonded water appeared at the surface areas much earlier, which  
35 could easily cause sample deformation and cracking. Overall, the experimental results suggest the  
36 capillary effects could play a major role at the first stage of slow drying at fiber level; then, the transfers  
37 between bound and free water could play a significant power source in the second drying stage. It is  
38 expected that this study will be of help in providing a basis to study and simulate the drying  
39 characteristics of cellular and hydrophilic materials.

40

41 **Keywords:**

42 Wood, air drying, water transport dynamics, free and bound water, near-infrared hyperspectral imaging,  
43 principal component analysis, rapid and high spatial resolution

44

45 **1. Introduction:**

46 The study of wood–water relationship goes back over a century (Tiemann 1906). Water has unique  
47 properties caused by its distinct polar charge distribution, allowing it to form hydrogen bonds with  
48 neighboring molecules (Israelachvili and Wennerström 1996). Water in wood could be classified as  
49 either free or bound water since the water vapor concentration could be negligible (Konopka and  
50 Kaliske 2018). Here, free water is considered as liquid water located in the lumens and intercellular  
51 spaces of the wood. In contrast, the water held by intermolecular forces between the major chemical  
52 components of wood cell walls is called bound water (Yang et al. 2014). Such bound water has profound  
53 effects on its physical properties, such as strength and stiffness (Mannes et al. 2009; Wagner et al. 2015)

54 Generally, water movement inside the wood during drying could include capillary flow (free water),  
55 diffusion as hygroscopic bound water, and diffusion as water vapor (Stamm 1964; Salin 2008). The  
56 capillary flow is generally used to explain the mechanism of water transpiration in standing trees (i.e.,  
57 cohesion–tension theory); i.e., a negative pressure caused by the evaporation pulls out liquid from the  
58 solid and moves it up through the xylem (Wheeler and Stroock 2008). Additionally, bound and free  
59 water transfer could also play a significant role in the interaction of wood with water (Zhou et al. 2018).  
60 Previous study indicated that free water in voids could be withdrawn from the sample mainly by  
61 capillary forces at the first drying stage, and the diffusion of vapor and bound water through the sample  
62 happens in the second drying stage from wet or fresh-cut wood (Salin 2008). However, the detailed  
63 characteristics of these two phases are not well identified (Penvern et al. 2020). Besides, substantial  
64 efforts have been devoted to constructing mathematical models of wood drying to simulate the mass  
65 transfer phenomena (Sun et al. 2000; Stanish 2008; Zhao et al. 2016; Varnier et al. 2020). Model  
66 validation remains challenging because the pathways of liquid water flow may differ between wood  
67 species, owing to the different moisture distribution in the anatomical structure of wood (Möttönen et  
68 al. 2011). This suggests that advanced moisture visualization techniques are required to study the drying  
69 characteristics of cellular and hydrophilic wood materials, as well as to support modern computational  
70 model constructions of wood drying (Nguyen et al. 2021).

71 Neutron radiography (Sedighi-Gilani et al. 2012) and X-ray tomography scanning (Wei et al. 2011;  
72 Sandberg and Salin 2012) have been well conducted to measure water content in wood. Additionally,  
73 nuclear magnetic resonance (NMR) spectroscopy (Almeida et al. 2007; Bonnet et al. 2017; Zhou et al.  
74 2018), time-domain NMR (Li et al. 2017; Wang et al. 2018), and magnetic resonance imaging (Almeida  
75 et al. 2008; Dvinskikh et al. 2011; Zhou et al. 2018) have been conducted to measure the free and bound  
76 water components. Near-infrared (NIR; wavelength range: 800–2500 nm) spectroscopy is another  
77 proven method for evaluating liquid water by mass (Tsuchikawa and Kobori 2015) and molecular  
78 dynamics in pure water (Segtnan et al. 2001) since vibrational NIR spectra contain information about  
79 the light absorbance of oxygen and hydrogen (O–H) structures in the analyzed samples (Kuroki et al.  
80 2019). Although overlapping NIR bands appear nonspecific and poorly resolved, they can be  
81 qualitatively evaluated by multivariate calibration algorithms and statistical methods (Martens and

82 Tormod 1992). NIR hyperspectral imaging (HSI) is an advanced technique for enabling comprehensive  
83 evaluation across the entire sample surface via utilizing spectral information in combination with the  
84 image data. The NIR-HSI is rapidly expanding in wood-related research to examine how a property  
85 varies spatially, such as for chemical composition (Thumm et al. 2010; Colares et al. 2016), wood  
86 density (Fernandes et al. 2013; Ma et al. 2017), and moisture content (MC) (Kobori et al. 2013). It is  
87 characterized with rapid speed, high spatial resolution, relatively less cost, and could quantify the water  
88 correctly even below the fiber saturation point (FSP) (Ma et al. 2021). Taking such advantages, the  
89 NIR-HSI has been evaluated to visualize the dynamic changing characteristics of free and hydrogen-  
90 bonded water over the wood cross-section with 5 mm thickness by analyzing the variance of HSI data  
91 between 1340 and 1610 nm (Ma et al. 2020). The experimental results encouraged a further study on  
92 water transport dynamics within wood under various sample sizes and drying temperatures. To achieve  
93 this goal, firstly, challenged by the penetration depth of the NIR light, as only several millimeters of  
94 wood samples could be evaluated (Ma et al. 2018). Additionally, because the NIR-HSI technique  
95 usually has a lower spectral resolution than traditional spectrometers, the wavelength selection and the  
96 stability of the prediction models must be developed.

97 Overall, this study aimed at visualizing the water distribution and its dynamics state of free and  
98 hydrogen-bonded water in wood with different sample lengths and dried at various temperatures.  
99 Sample thickness was selected as 4 mm to first evaluate MC model construction for wood transverse  
100 section. Then, we visualize the water movement characteristics in the wood samples during the drying  
101 process by cutting them along the grain. Finally, the drying characteristics will be discussed in detail  
102 based on the MC visualization results. This study is expected to be of help in providing a basis to study  
103 the drying characteristics in cellular and hydrophilic materials.

104

## 105 **2. Material and methods**

### 106 ***2.1 Sample preparation***

107 Japanese cypress (*Chamaecyparis obtusa*) was used as an experimental sample in this study. The  
108 wood samples were commercially purchased from a local wood processing company and initially air-  
109 dried at ambient conditions for one month. For moisture content prediction model calibration, the

110 dimensions of 90 samples were adjusted to 20 (Longitudinal (L)) × 15 (Tangential (T)) × 4 (Radial (R))  
111 mm. The appearance of the sample is shown in Fig. 1 (a<sub>1</sub>). For the MC mapping test, the dimensions  
112 were divided into three types according to the length in the fiber direction: 30, 60, or 90 (L) × 30 (T) ×  
113 30 (R) mm (Fig. 1 (a<sub>2</sub>)). Each type included 12 samples dried at different temperatures. All samples  
114 were taken from sapwood and side by side to minimize the variability between them.

115

## 116 **2.2 NIR hyperspectral images collection**

117 NIR hyperspectral images were acquired using a push-broom line scanning system (Compovision,  
118 Sumitomo Electric Industries, Ltd., Osaka, Japan), as shown in Fig. 1 (b<sub>1-2</sub>). The camera possesses a  
119 spectroscope and a two-dimensional photosensitive element capable of receiving NIR light from 1002  
120 to 2350 nm at a spectral resolution of approximately 6.2 nm. The distance between the target and the  
121 camera was manually adjusted to achieve a horizontal field view of 40 mm (with a spatial interval of  
122 approximately 125 μm/pixel). A tube-shaped halogen light source at 45° was used as the source of  
123 illumination. Each sample was positioned on a moving slider, and spectral data were scanned line by  
124 line. The exposure time was 4.5 ms (frame rate: 200 frames/s). One scan was measured for each sample  
125 at a specific MC condition (scan speed: 25 mm/s); A white plate was photographed under the same  
126 conditions. Dark images were obtained by turning off the light source and completely covering the lens  
127 with its cap. All the collected spectral images of the wood samples were then converted to relative  
128 diffuse reflectance values for further partial least squares (PLS) regression analysis using Eq. 1:

$$129 \quad R_{\lambda,n} = \frac{S_{\lambda,n} - D_{\lambda,n}}{B_{\lambda,n} - D_{\lambda,n}} \quad \text{Eq. 1}$$

130 where  $\lambda$  and  $n$  denote the wavelength and pixel index variable, respectively.  $S$  and  $B$  are samples and a  
131 white reference image, respectively.  $D$  is the dark image.

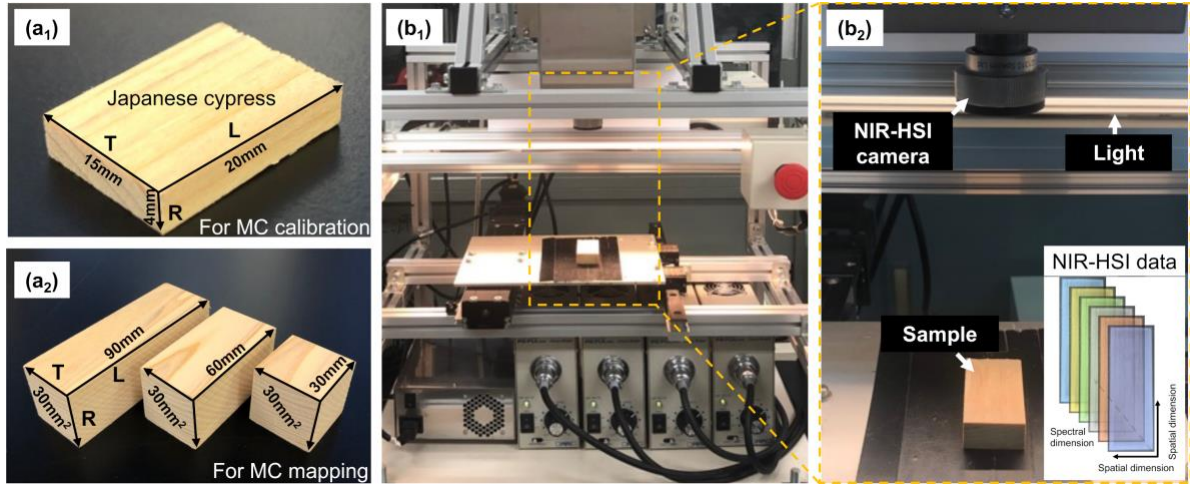


**Fig. 1** Sample preparation and the NIR-HSI system used in this study mainly contains an HSI camera, tube-shaped halogen light source, and sample moving slider.

132

### 133 2.3 MC reference value measurement

134 The steps of the MC reference measurement for calibration model constructions are shown in Fig.  
 135 2 (a<sub>1</sub>). Air-dried wood samples were placed in a low-pressure desiccator for 24 h to fully absorb water.  
 136 Then, the sample weights and their hyperspectral images (LT surface) were simultaneously measured  
 137 at different air-drying stages. The sample weight was taken as the average weight before and after the  
 138 NIR-HSI data measurement. Finally, all samples were sufficiently dried in an oven (103 °C, 48 h), and  
 139 the dried weight was measured to calculate moisture content values as follows:

$$140 \quad MC (\%) = \left( \frac{(w_b + w_a) - w_d}{2} \right) \quad \text{Eq. 2}$$

141 where  $w_b$  and  $w_a$  are the weights before and after image acquisition, respectively, and  $w_d$  is the reference  
 142 weight after oven-drying.

143 The steps of the MC mapping test are shown in Fig. 2 (b<sub>1</sub>). Each sample was sealed with commercial  
 144 aluminum tape along the four vertical sides parallel to the imbibition direction to reduce the effects  
 145 caused by the large MC drop at the sample four-edge surfaces (RL and TL). Then, to observe the effect  
 146 of the drying temperature on the moisture transfer characteristics, oven-drying was performed under  
 147 three temperatures (30 °C, 60 °C, and 90 °C) without wind. The drying time was divided stepwise  
 148 between the samples to achieve approximately the same MC for the samples dried at different

149 temperatures (100%, 60%, and 20%). After peeling off the aluminum tape, each sample was  
150 immediately cut parallel to the LT plane; then, the hyperspectral images were collected from the cut  
151 surface.

152

#### 153 **2.4 MC prediction model construction by partial least squares (PLS) analysis**

154 In this study, the averaged MCs of the samples were used to calibrate the averaged NIR spectra  
155 collected from each entire sample (Fig. 2 (a<sub>2</sub>)). A subset of 70 % of all the measured data was randomly  
156 selected as a calibration set during the PLS regression model development, leaving 30 % for a test set.  
157 Standard normal variate (SNV) spectral pretreatments were first used to correct the baseline shifts  
158 mainly caused by light scattering (Kobori et al. 2013). Additionally, leave-one-out cross-validation was  
159 used to optimize the best number of latent variables (LVs). The performance of the constructed  
160 calibration model was characterized by the coefficient of determination ( $R^2$ ) and root mean squared  
161 error (RMSE):

$$162 \quad R^2 = 1 - \frac{\sum_{i=1}^n (y_i - \hat{y}_i)^2}{\sum_{i=1}^n (y_i - \bar{y})^2} \quad \text{Eq. 3}$$

$$163 \quad \text{RMSE} = \sqrt{\frac{1}{n} \sum_{i=1}^n (\hat{y}_i - y_i)^2} \quad \text{Eq. 4}$$

164 where  $n$  is the number of measurements,  $y$  is the MC reference values,  $\hat{y}$  are their values predicted by  
165 the PLS regression analysis, and  $\bar{y}$  is the mean values of the  $y$ .

166 The spectrum contained in each pixel of the obtained NIR-HSI data was then subjected to the same  
167 pretreatments, and the PLS prediction model was applied to build the MC mapping images (Fig. 2 (b<sub>2</sub>)).

168

#### 169 **2.5 Visualizing the dynamic state of free and bound water by principal component analysis (PCA)**

170 PCA has been used to utilize the state-changing of free and bound water distribution because it is a  
171 valuable tool for characterizing spectral data variance and dimension reduction (Martens and Tormod  
172 1992; Watanabe et al. 2006). For spectral pretreatments: first, the measured average reflection spectrum  
173 was converted into absorbance and only the wavelength region of the peak attributed to O–H (1854–  
174 2092 nm) was selected. Next, the spectra of all-dry wood were subtracted from the spectra collected at  
175 various MC levels. Additionally, baseline correction was conducted by differentiating the straight lines

176 connecting both ends of the peak (Fig. 2 (a<sub>2</sub>)). After PCA, the spectrum of each pixel of the obtained  
 177 NIR-HSI image was then subjected to the same pretreatments, and the PC loadings were used to earn  
 178 the PC scores for checking the distribution of free and bound water inside the wood samples (Fig. 2  
 179 (b<sub>2</sub>)). In this study, Matlab (The MathWorks Inc., Natick, MA, USA) was used for data analysis and  
 180 image processing.

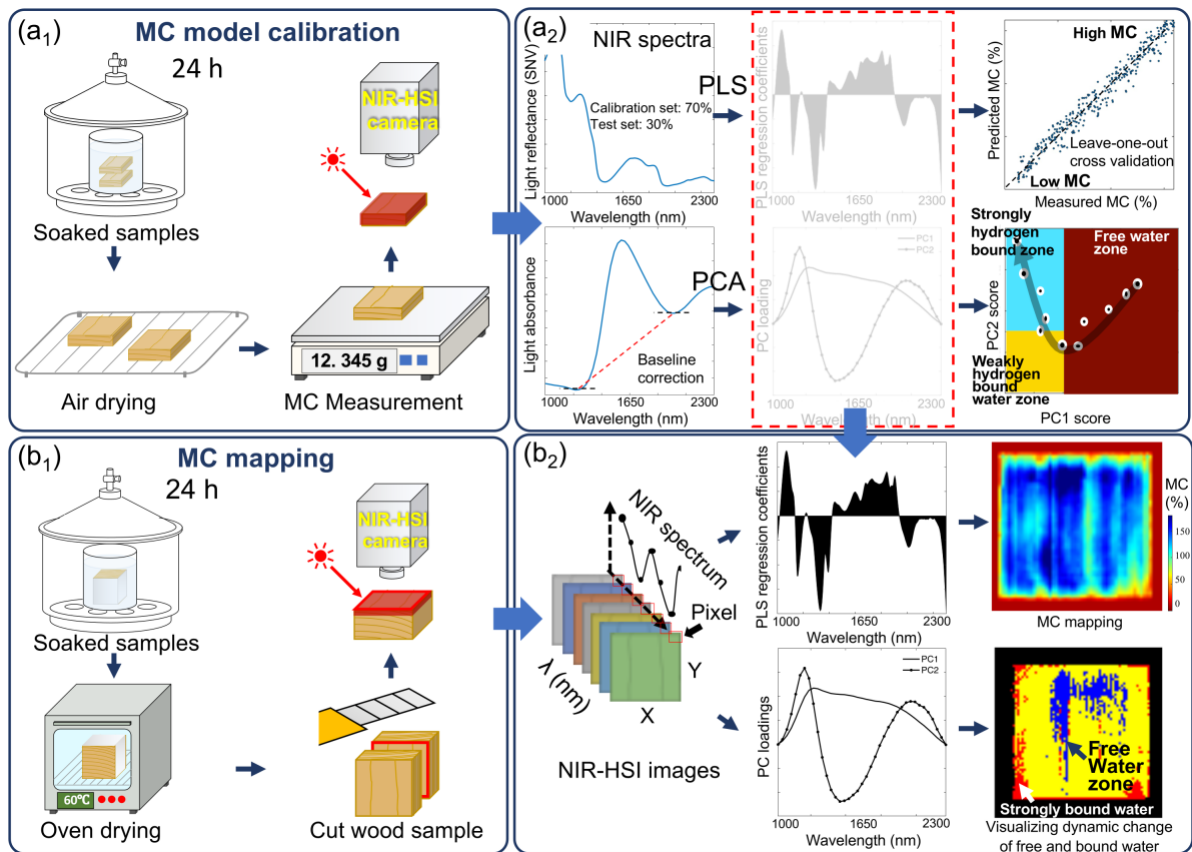


**Fig.2 NIR hyperspectral images collection and imaging analysis for MC prediction model construction (a<sub>1-2</sub>) and MC mapping (b<sub>1-2</sub>).**

181

182 **3. Results and discussion:**

183 **3.1 MC prediction model construction by PLS regression analysis**

184 The raw NIR spectral data of the wood samples with averaged MC from 214.77% to 12.57% are  
 185 shown in Fig. 3(a). Logically, the overall light reflectance increases with decreasing MC. Water bands  
 186 close to 1450 nm are the vibrational absorption bands of the O–H and C–H groups. Additionally, water  
 187 bands close to 1930 nm correspond to water absorption (Schwanninger et al. 2011). It is evident that  
 188 the region near 1930 nm had a sharper light absorption peak than 1450 nm, which should be effectively

189 collected and used for the study of water. SNV spectral pretreatment was used to correct for the baseline  
190 offset before MC calibration Fig. 3(b).

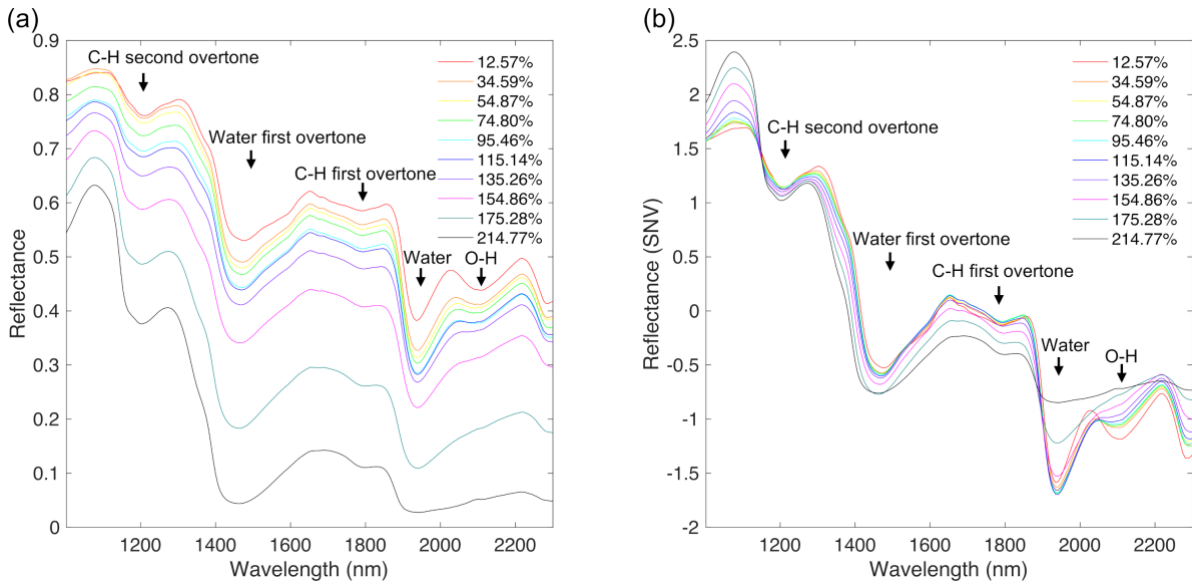


**Fig. 3 Averaged NIR spectral data (1002–2300 nm) of Japanese cypress before (a) and after (b) SNV spectral pretreatment.**

191

192 Fig. 4(a) shows approximately 99% of the variance in the calibration spectra could be explained  
193 by five principal components. Fig. 4(b) shows the RMSE of the predictors and response; The LV  
194 number 5 was selected with a bit lower prediction accuracy against over-fitting. Fig. 4(c) shows the  
195 PLS regression coefficients with respect to the averaged NIR spectra Fig. 3(b). The relatively low  
196 absolute values without large fluctuations, suggesting a strong correlation between the MC reference  
197 values and the averaged NIR spectra.

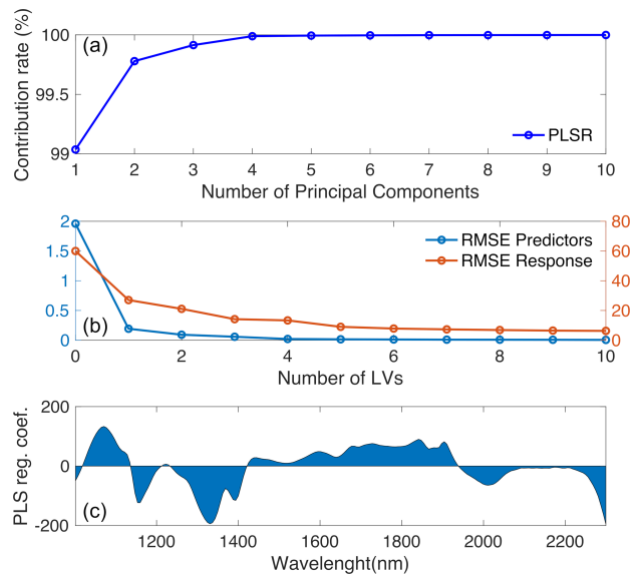


**Fig. 4 (a) Percent variance explained in X, (b) the RMSE of predictors and response, (c) the PLS regression coefficients.**

198

199 Fig. 5 shows the relationship between the measured MC reference values and the predicted MC  
 200 values by the averaged NIR spectra. The summary of MC reference values (%) for PLS calibration and  
 201 their prediction results are shown in Table 1. The denominator is the dry weight, and the MC calculated  
 202 in this way can exceed 100%. Overall, the PLS calibration model achieved a high prediction accuracy:  
 203 the  $R^2_{Cal}$  and  $RMSE_{Cal}$  were 0.98 and 8.81%, respectively. For an independent test set, the  $R^2_{Test}$  was  
 204 0.97 with an  $RMSE_{Test}$  of 10.11%. Comparing the results with previous studies (Kobori et al. 2013; Ma  
 205 et al. 2020), in which the transversal section was scanned, there is a marked reduction in the MC  
 206 prediction accuracy. This may be explained by the fact that the incident radiation directly interferes  
 207 with the free water present in the lumen of the cell when scanning the transverse section (Tsuchikawa  
 208 et al. 1996). The NIR spectra collected on transversal sections were also experimentally confirmed to  
 209 be better than models based on the spectra collected from tangential or radial sections of red oak (Defo  
 210 et al. 2007).

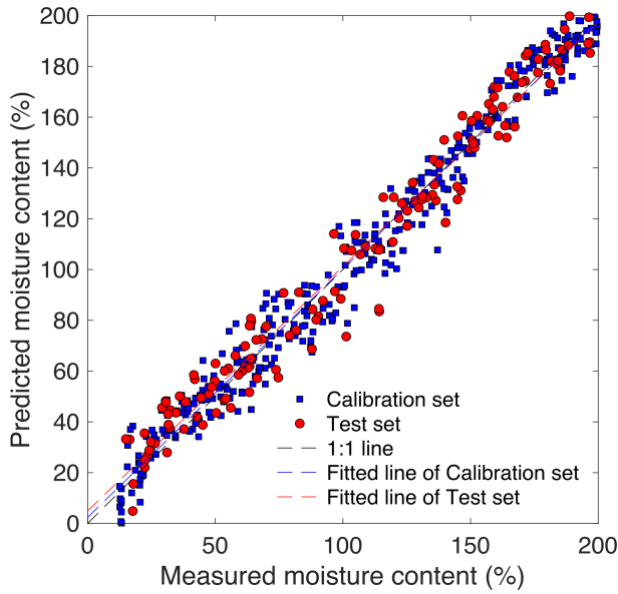


**Fig. 5 Scatterplot of the measured and predicted MC values by NIR-HSI method.**

211 **Table 1: PLS regression results for MC (%).**

Calibration set						Test set					
n	Range (%)	Mean (%)	SD (%)	RMSE <sub>cal</sub> (%)	$R^2_{cal}$	n	Range (%)	Mean (%)	SD (%)	RMSE <sub>test</sub> (%)	$R^2_{test}$
371	12.60-214.77	111.34	59.32	8.81	0.98	159	12.57-213.73	111.46	60.20	10.11	0.97

SD: standard deviation; RMSE: root mean square error;  $R^2$ : coefficient of determination.

212

213 **3.2 Visualizing the MC changes in the wood samples**

214 Fig. 6(a) shows the MC mapping results of the internal wood LT surface. They have been slowly  
 215 dried at the same temperature of 30 °C, and the moisture transfer characteristics by size can be  
 216 compared. Although it is notable that the mapping results were from different samples (since after  
 217 cutting, the same sample could not be continuously used), some water transport characteristics can be  
 218 confirmed. Firstly, a sharp decrease in MC was confirmed from the initial stage of drying near the wood  
 219 surface. The length of this part did not change at various sample lengths: approximately 2–3 mm from  
 220 each sample surface, which is close to the length of the sample tracheid cell, approximately 3.5 mm  
 221 (Yokoyama et al. 2011). It suggests that the tracheid cells near the surface were firstly dried; such a  
 222 phenomenon was also found in previous works (Wiberg 1995; Wiberg and Morén 1999; Xu et al. 2017)

223 for the samples still with a high averaged MC. One of the most intriguing findings is that the subsurface  
224 areas tended to have higher MC than inside areas after drying for several hours (i.e., at 100% and 60%  
225 reference MC), especially inside longer wood samples. It suggests that the evaporation of water from  
226 the wood surface causes pressure differences during drying (i.e., the driving force of free water), and  
227 the capillary forces could exert a pull on the free water in the interior parts (Booker, R 1996; Wiberg  
228 and Morén 1999). Such a phenomenon was not evident for shorter samples, suggesting that the sample  
229 length affects the water distribution inside the wood during drying.

230 The next question arising is how a change in external climate affects the redistribution of water in  
231 the interior parts of the sample; the MC mapping results at different drying temperatures were  
232 compared. When increasing the drying temperature from 30°C to 60°C and 90°C, there is an apparent  
233 tendency for water in wood to be more evenly distributed. It may be caused by that the cohesive force  
234 between water molecules was weakened by the temperature rise as the thermal motion of the molecules  
235 increased (Chaplin 2010), and the vapor pressure inside the wood could also be increased by the  
236 temperature (Hunter and Sutherland 1997). Subsequently, the speed of water movement inside the wood  
237 could be faster than drying at lower temperatures. Although thermal expansion can also be another  
238 important factor to cause moisture flow variations and consequently hygroscopic deformations occur,  
239 such effects might very well be negligible compared to hygroscopic effects (Goli et al. 2019).

240 When the average MC dropped to approximately 20% by all drying temperatures, although the  
241 average and the surface MC decreased to below FSP, the central region was still higher than FSP. It  
242 suggests that the diffusion of bound water and vapor from the deeper parts forward to the surface of  
243 wood samples started to dominate the MC change (Xu et al. 2017). The cracks were found in the samples  
244 that were dried at 60°C and 90°C, which is most likely attributable to the difference in the shrinkage  
245 between the inside of the wood and the vicinity of the wood surface.

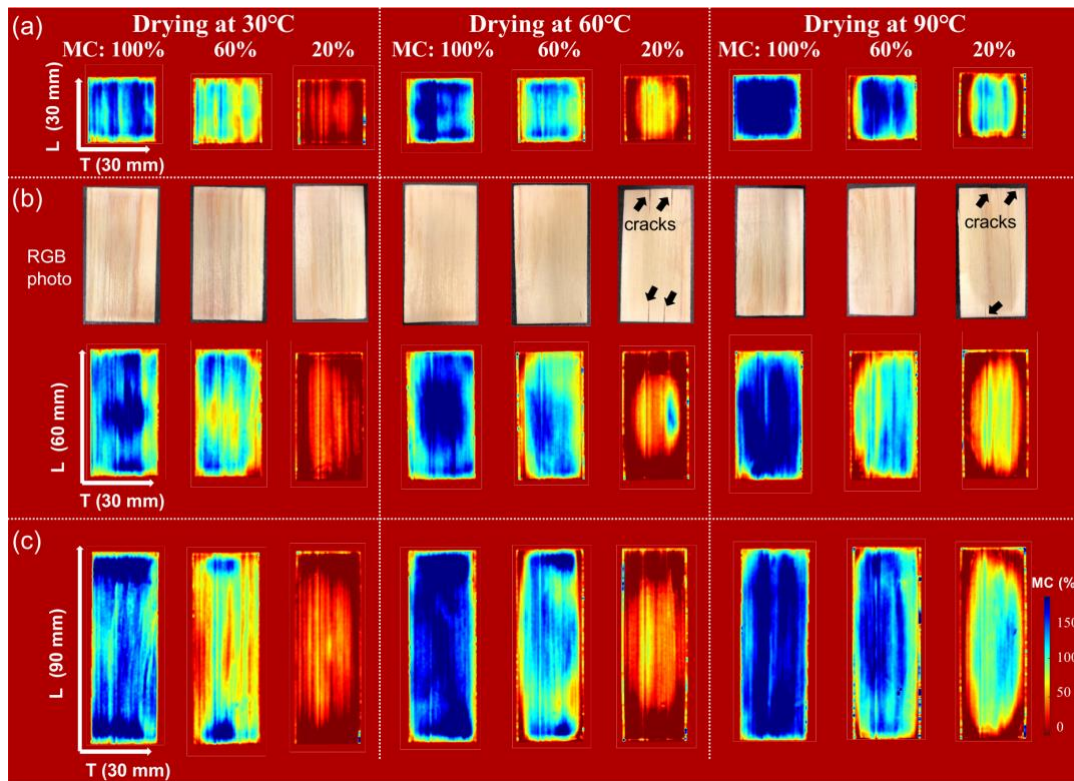


**Fig. 6** Moisture content distribution in the wood samples with different lengths (a: 30 mm, b: 60 mm, and c: 90 mm) and drying at various temperatures.

246

### 247 3.3 Water-wood hydrogen bonding properties characterizing by PCA

248 Fig. 7(a) shows the difference spectra between 1853 and 2092 nm; it is evident that the absorption  
 249 peak shifted to longer wavelengths during drying, suggesting that the mobility of water decreased (i.e.,  
 250 the percentage of bound water increased). The loading spectra of the first two principal components are  
 251 shown in Fig. 7(b). It shows that the PC1 scores become positively enormous in places where the MC  
 252 of the wood wildly fluctuates and are considered to represent the mass of the MC. Since the PC2 scores  
 253 become positively and negatively extensive in the hydrogen-bonding O–H region, it could be  
 254 considered to represent the characteristics of hydrogen-bonding properties. The three curves can be  
 255 interpreted as follows: (1) the positive peak at wavelengths around 1891 nm could be due to free water,  
 256 (2) the negative peak at 1942 nm may correlate with weakly bound water with hindered mobility, and  
 257 (3) the positive peak at approximately 2042 nm could correspond to water that is strongly hydrogen-  
 258 bonded with the wood cell wall. Fig. 7(c) shows the first and the second PC scores obtained by PCA.

259 In PC2, the score decreased as the free water decreased. Additionally, the score increased as the bound  
 260 water increased. Based on this, the PCA score plot shows that free water is sufficiently high on the right  
 261 region, whereas free water decreases and the proportion of bound water increases on the left region. As  
 262 a result, a hydrogen bond prediction model was constructed in which scores were obtained using the  
 263 loading of PC1 and PC2, and the region of the score plot predicted hydrogen bendability.

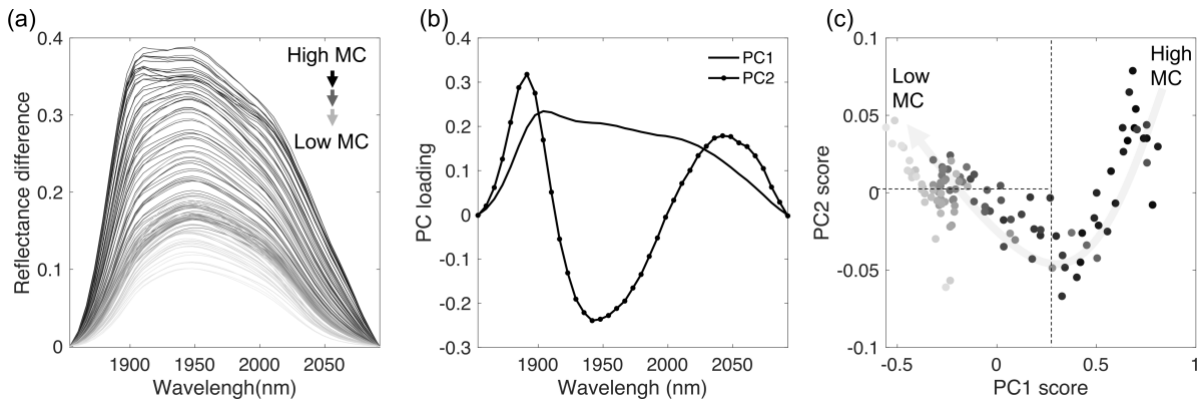


**Fig. 7 (a) Different spectra collected from representative MCs (dark to light color means from high MC to low MC). (b) First two PC loadings. (c) Scatterplot of the first two PC scores (dark to light color means from high MC to low MC).**

264

### 265 3.4 Visualizing the dynamic change of free water and bound water in wood samples

266 The PC1 and PC2 score mapping results of the same wood samples of Fig.6 are shown in Fig. 8.  
 267 These imaging results are consistent with the discussion presented in Fig. 7. PC1 and PC2 mapping  
 268 scores support an understanding of free and bound water distribution in each sample.

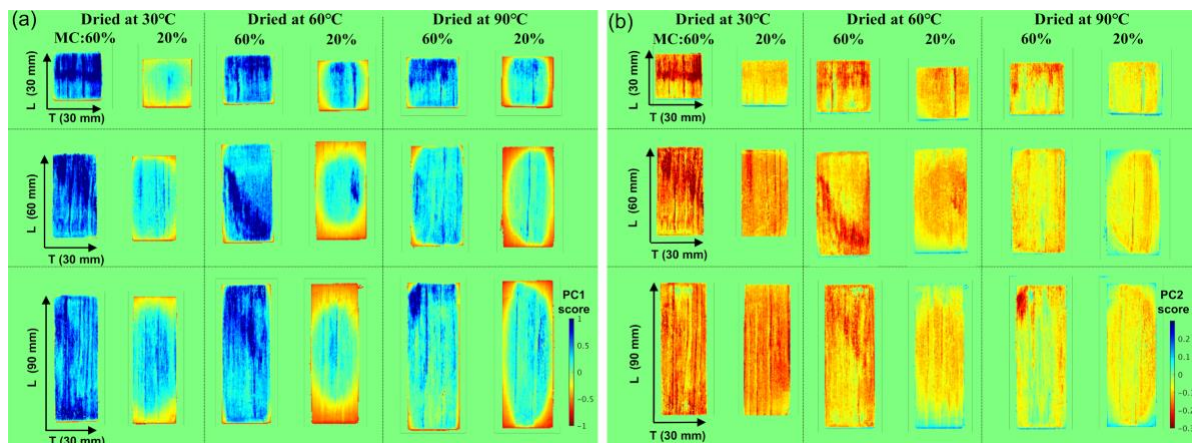


**Fig. 8 PC1 (a) and PC2 (b) score mapping results of the same wood samples as Fig. 6.**

269

270 The classification results based on their PC1 and PC2 scores (F: free water mainly dehydrates; W:  
271 weakly bound water dehydrates; and S: stronger bound water in wood cell wall starts to dehydrate) are  
272 shown in Fig. 9. Compared to drying at higher temperatures, a relatively constant drying rate and a  
273 homogeneous distribution of the water content throughout the material occurred for slow drying at a  
274 temperature of 30°C. It suggests that the evaporated bound water near the sample surface could be  
275 effectively replaced by the absorption of deeper/around free water, which could be the power source to  
276 control imbibition in wood rather than capillarity in this second drying stage. The finding here is  
277 comparable with the results from a published study (Penvern et al. 2020); i.e., the transfers between  
278 bound and free water could play a major role in the interaction of wood with water during drying.

279 The diffusion of bound water could be reduced by increasing the drying temperature (Penvern et al.  
280 2020). The mapping results show that a significant gradient of water concentration develops toward the  
281 interior of the sample dried at 60 °C and 90 °C compared to that dried at 30 °C. It suggests that the  
282 velocity of water transport by diffusion in cell walls was too slow to replace the bound water extracted  
283 by evaporation along the free surface. It caused wood shrinkage due to a decrease in bound water, and  
284 cracks occurred due to the difference in the shrinkage between the inside of the wood and the vicinity  
285 of the wood surface (Fig. 6). There may be a possibility that drying the outside (e.g., oven-drying in  
286 this study) and inside (e.g., microwave drying (Du et al. 2005)) of the wood samples together may  
287 provide decreased drying time and still maintain end-product quality, more work is needed to prove  
288 this.

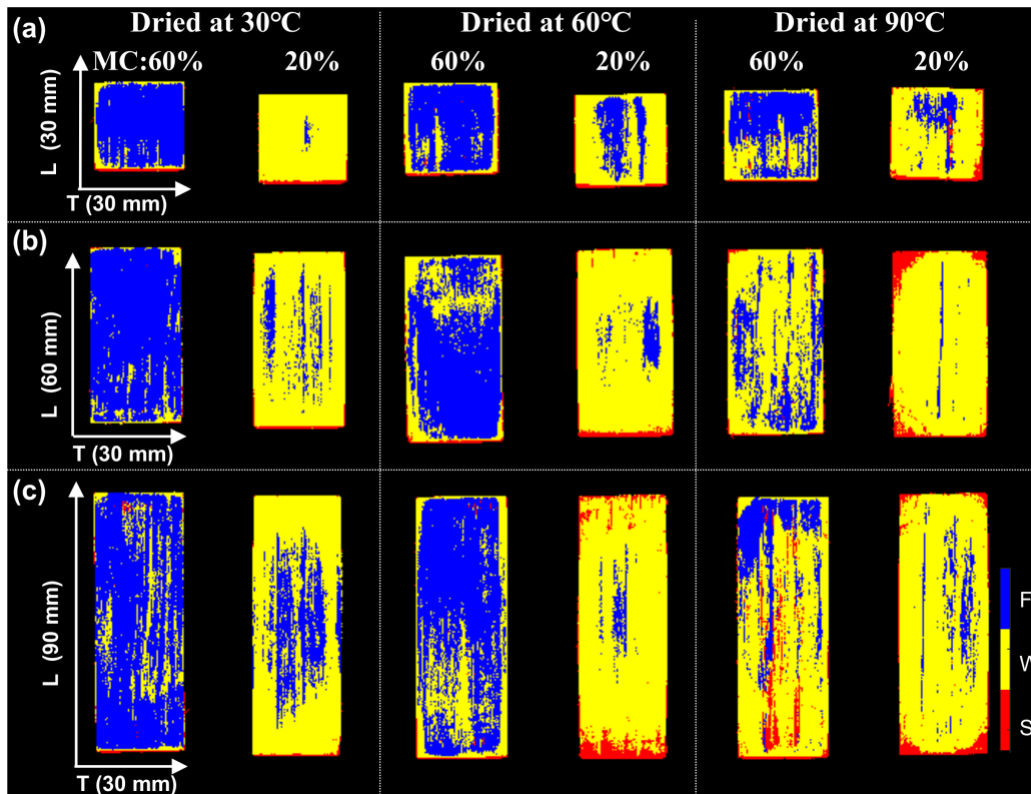


**Fig. 9. Dynamic change of free water and bound water inside wood samples with different lengths and dried at various temperatures (F: free water mainly dehydrates; W: weakly bound water dehydrates; and S: stronger bound water in wood cell wall starts to dehydrate).**

289

290 **Conclusions:**

291 This study aims to study the water transport dynamic inside wood with different lengths and at  
 292 various drying temperatures by long-wave near-infrared hyperspectral imaging. From the MC mapping  
 293 results earned by the PLS regression analysis, the area near the subsurface of the wood samples tends  
 294 to have higher MC than the central parts during drying at lower temperatures, especially in the case of  
 295 longer wood samples. For drying at higher temperatures, strongly bonded water appeared at the surface  
 296 areas much earlier, which could easily cause sample deformation and cracking. Overall, the  
 297 experimental results suggest the capillary effects could play a major role at the first stage of slow drying  
 298 at fiber level; then, the transfers between bound and free water could play a significant power source in  
 299 the second drying stage.

300 The particular advantage arising from the NIR-HSI method is that the changes of moisture  
301 (MC/moisture-binding) in the sample could be visualized almost real-time with a high spatial resolution.  
302 Additionally, it can provide information on the O–H vibration speed, i.e., bound water. It should also  
303 concern further studies on the water transport in other wood types with 3D water distribution  
304 characteristics. Hopefully, such NIR-HSI based MC mapping results could be used as a basis to study  
305 the water movement in cellular and hydrophilic materials and further validate mechanical MC transport  
306 simulation models.

307

#### 308 **4. Acknowledgment**

309 The authors are grateful for the financial support provided by JSPS (KAKENHI, no. 19K15886).

310 **5. Reference:**

- 311 Almeida G, Gagné S, Hernández RE (2007) A NMR study of water distribution in hardwoods at  
312 several equilibrium moisture contents. *Wood Sci Technol* 41:293–307.  
313 <https://doi.org/10.1007/s00226-006-0116-3>
- 314 Almeida G, Leclerc S, Perre P (2008) NMR imaging of fluid pathways during drainage of  
315 softwood in a pressure membrane chamber. *Int J Multiph Flow* 34:312–321.  
316 <https://doi.org/10.1016/j.ijmultiphaseflow.2007.10.009>
- 317 Bonnet M, Courtier-Murias D, Faure P, et al (2017) NMR determination of sorption isotherms  
318 in earlywood and latewood of Douglas fir. Identification of bound water components  
319 related to their local environment. *Holzforschung* 71:481–490. [https://doi.org/10.1515/hf-](https://doi.org/10.1515/hf-2016-0152)  
320 [2016-0152](https://doi.org/10.1515/hf-2016-0152)
- 321 Booker, R E (1996) New theories for liquid water flow in wood. 5th Int IUFRO Wood Dry Conf  
322 Quebec City, Quebec, Canada
- 323 Chaplin MF (2010) Water's hydrogen bond strength. *Water Life Unique Prop H2O* 69–86.  
324 <https://doi.org/10.1201/EBK1439803561>
- 325 Colares CJG, Pastore TCM, Coradin VTR, et al (2016) Near infrared hyperspectral imaging and  
326 MCR-ALS applied for mapping chemical composition of the wood species *Swietenia*  
327 *Macrophylla* King (Mahogany) at microscopic level. *Microchem J* 124:356–363.  
328 <https://doi.org/10.1016/j.microc.2015.09.022>
- 329 Defo M, Taylor AM, Bond B (2007) Determination of moisture content and density of fresh-  
330 sawn red oak lumber by near infrared spectroscopy. *For Prod J* 57:68–72
- 331 Du G, Wang S, Cai Z (2005) Microwave drying of wood strands. *Dry Technol* 23:2421–2436.  
332 <https://doi.org/10.1080/07373930500340494>

333 Dvinskikh S V., Henriksson M, Berglund LA, Furó I (2011) A multinuclear magnetic resonance  
334 imaging (MRI) study of wood with adsorbed water: Estimating bound water concentration  
335 and local wood density. *Holzforschung* 65:103–107. <https://doi.org/10.1515/HF.2010.121>

336 Fernandes A, Lousada J, Morais J, et al (2013) Measurement of intra-ring wood density by  
337 means of imaging VIS/NIR spectroscopy (hyperspectral imaging). *Holzforschung* 67:59–  
338 65. <https://doi.org/10.1515/hf-2011-0258>

339 Goli G, Becherini F, Di Tuccio MC, et al (2019) Thermal expansion of wood at different  
340 equilibrium moisture contents. *J Wood Sci* 65:. <https://doi.org/10.1186/s10086-019-1781-9>

341 Hunter AJ, Sutherland JW (1997) The evaporation of water from wood at high temperatures.  
342 *Wood Sci Technol* 31:73–76. <https://doi.org/10.1007/BF00705922>

343 Israelachvili J, Wennerström H (1996) Role of hydration and water structure in biological and  
344 colloidal interactions. *Nature* 379:219–225. <https://doi.org/10.1038/379219a0>

345 Kobori H, Gorretta N, Rabatel G, et al (2013) Applicability of Vis-NIR hyperspectral imaging  
346 for monitoring wood moisture content (MC). *Holzforschung* 67:307–314.  
347 <https://doi.org/10.1515/hf-2012-0054>

348 Konopka D, Kaliske M (2018) Transient multi-FICKian hygro-mechanical analysis of wood.  
349 *Comput Struct* 197:12–27. <https://doi.org/10.1016/j.compstruc.2017.11.012>

350 Kuroki S, Tsenkova R, Moyankova D, et al (2019) Water molecular structure underpins  
351 extreme desiccation tolerance of the resurrection plant *Haberlea rhodopensis*. *Sci Rep* 9:1–  
352 12. <https://doi.org/10.1038/s41598-019-39443-4>

353 Li X, Gao Y, Zhang M, et al (2017) Water migration in poplar wood during microwave drying  
354 studied by time domain nuclear magnetic resonance (TD-NMR). *Holzforschung* 71:881–  
355 887. <https://doi.org/10.1515/hf-2017-0040>

356 Ma T, Inagaki T, Tsuchikawa S (2017) Calibration of SilviScan data of *Cryptomeria japonica*  
357 wood concerning density and microfibril angles with NIR hyperspectral imaging with high  
358 spatial resolution. *Holzforschung* 71:341–347. <https://doi.org/10.1515/hf-2016-0153>

359 Ma T, Inagaki T, Tsuchikawa S (2020) Rapidly visualizing the dynamic state of free, weakly,  
360 and strongly hydrogen-bonded water with lignocellulosic material during drying by near-  
361 infrared hyperspectral imaging. *Cellulose* 27:4857–4869. [https://doi.org/10.1007/s10570-](https://doi.org/10.1007/s10570-020-03117-6)  
362 [020-03117-6](https://doi.org/10.1007/s10570-020-03117-6)

363 Ma T, Schajer G, Inagaki T, et al (2018) Optical characteristics of Douglas fir at various  
364 densities, grain directions and thicknesses investigated by near-infrared spatially resolved  
365 spectroscopy (NIR-SRS). *Holzforschung* 1–8. <https://doi.org/10.1515/hf-2017-0213>

366 Ma T, Schimleck L, Inagaki T, Tsuchikawa S (2021) Rapid and nondestructive evaluation of  
367 hygroscopic behavior changes of thermally modified softwood and hardwood samples  
368 using near-infrared hyperspectral imaging (NIR-HSI). *Holzforschung* 75:345–357.  
369 <https://doi.org/10.1515/hf-2019-0298>

370 Mannes D, Sonderegger W, Hering S, et al (2009) Non-destructive determination and  
371 quantification of diffusion processes in wood by means of neutron imaging.  
372 *Holzforschung* 63:589–596. <https://doi.org/10.1515/HF.2009.100>

373 Martens H, Tormod N (1992) *Multivariate calibration*. John Wiley & Sons.

374 Möttönen V, Kärki T, Martikka O (2011) Method for determining liquid water flow in wood  
375 during drying using a fluorescent dye tracer. *Eur J Wood Wood Prod* 69:287–293.  
376 <https://doi.org/10.1007/s00107-010-0424-z>

377 Nguyen DM, Almeida G, Nguyen TML, et al (2021) A Critical Review of Current Imaging  
378 Techniques to Investigate Water Transfers in Wood and Biosourced Materials. *Transp.*  
379 *Porous Media* 137:21–61

380 Penvern H, Zhou M, Maillet B, et al (2020) How Bound Water Regulates Wood Drying. *Phys*  
381 *Rev Appl* 14:1. <https://doi.org/10.1103/PhysRevApplied.14.054051>

382 Salin JG (2008) Drying of liquid water in wood as influenced by the capillary fiber network.  
383 *Dry Technol* 26:560–567. <https://doi.org/10.1080/07373930801944747>

384 Sandberg K, Salin JG (2012) Liquid water absorption in dried Norway spruce timber measured  
385 with CT scanning and viewed as a percolation process. *Wood Sci Technol* 46:207–219.  
386 <https://doi.org/10.1007/s00226-010-0371-1>

387 Schwanninger M, Rodrigues JC, Fackler K (2011) A review of band assignments in near  
388 infrared spectra of wood and wood components. *J Near Infrared Spectrosc* 19:287–308.  
389 <https://doi.org/10.1255/jnirs.955>

390 Sedighi-Gilani M, Griffa M, Mannes D, et al (2012) Visualization and quantification of liquid  
391 water transport in softwood by means of neutron radiography. *Int J Heat Mass Transf*  
392 55:6211–6221. <https://doi.org/10.1016/j.ijheatmasstransfer.2012.06.045>

393 Segtnan VH, Šašić Š, Isaksson T, Ozaki Y (2001) Studies on the structure of water using two-  
394 dimensional near-infrared correlation spectroscopy and principal component analysis.  
395 *Anal Chem* 73:3153–3161. <https://doi.org/10.1021/ac010102n>

396 Stamm AJ (1964) Wood and cellulose science. *Wood Cellul Sci* 245

397 Stanish MA (2008) Application of wood drying simulation models in commercial lumber  
398 manufacturing. *Dry Technol* 26:1089–1096. <https://doi.org/10.1080/07373930802266033>

399 Sun ZF, Carrington CG, Bannister P (2000) Dynamic modelling of the wood stack in a wood  
400 drying kiln. *Chem Eng Res Des* 78:107–117. <https://doi.org/10.1205/026387600526942>

401 Thumm A, Riddell M, Nanayakkara B, et al (2010) Near infrared hyperspectral imaging applied  
402 to mapping chemical composition in wood samples. *J Near Infrared Spectrosc* 18:507–  
403 515. <https://doi.org/10.1255/jnirs.909>

404 Tiemann HD (1906) Effect of moisture upon the strength and stiffness of wood. US Department  
405 of Agriculture, Forest Service

406 Tsuchikawa S, Hayashi K, Tsutsumi S (1996) Nondestructive Measurement of the Subsurface  
407 Structure of Biological Material Having Cellular Structure by Using Near-Infrared  
408 Spectroscopy. *Appl Spectrosc* 50:1117–1124

409 Tsuchikawa S, Kobori H (2015) A review of recent application of near infrared spectroscopy to  
410 wood science and technology. *J Wood Sci* 61:213–220. [https://doi.org/10.1007/s10086-](https://doi.org/10.1007/s10086-015-1467-x)  
411 [015-1467-x](https://doi.org/10.1007/s10086-015-1467-x)

412 Varnier M, Sauvat N, Ulmet L, et al (2020) Influence of temperature in a mass transfer  
413 simulation: application to wood. *Wood Sci Technol* 54:943–962.  
414 <https://doi.org/10.1007/s00226-020-01197-y>

415 Wagner L, Bos C, Bader TK, de Borst K (2015) Effect of water on the mechanical properties of  
416 wood cell walls - Results of a nanoindentation study. *BioResources* 10:4011–4025.  
417 <https://doi.org/10.15376/biores.10.3.4011-4025>

418 Wang Z, Wang XM, Chen ZJ (2018) Water states and migration in Xinjiang poplar and  
419 Mongolian Scotch pine monitored by TD-NMR during drying. *Holzforschung* 72:113–  
420 123. <https://doi.org/10.1515/hf-2017-0033>

421 Watanabe A, Morita S, Ozaki Y (2006) A study on water adsorption onto microcrystalline  
422 cellulose by near-infrared spectroscopy with two-dimensional correlation spectroscopy  
423 and principal component analysis. *Appl Spectrosc* 60:1054–1061.  
424 <https://doi.org/10.1366/000370206778397452>

425 Wei Q, Leblon B, la Rocque A (2011) On the use of X-ray computed tomography for  
426 determining wood properties: A review. *Can J For Res* 41:2120–2140.  
427 <https://doi.org/10.1139/x11-111>

428 Wheeler TD, Stroock AD (2008) The transpiration of water at negative pressures in a synthetic  
429 tree. *Nature* 455:208–212. <https://doi.org/10.1038/nature07226>

430 Wiberg P (1995) Moisture distribution changes during drying. *Holz als Roh- und Werkst* 53:402

431 Wiberg P, Morén TJ (1999) Moisture flux determination in wood during drying above fibre  
432 saturation point using CT-scanning and digital image processing. *Holz als Roh - und*  
433 *Werkst* 57:137–144. <https://doi.org/10.1007/s001070050029>

434 Xu K, Lu J, Gao Y, et al (2017) Determination of moisture content and moisture content  
435 profiles in wood during drying by low-field nuclear magnetic resonance. *Dry Technol*  
436 35:1909–1918. <https://doi.org/10.1080/07373937.2017.1291519>

437 Yang S, Eom C, Han Y, et al (2014) Near-infrared spectroscopic analysis for classification of  
438 water molecules in wood by a theory of water mixtures. *Wood Fiber Sci* 46:138–147

439 Yokoyama M, Gril J, Matsuo M, et al (2011) Mechanical characteristics of aged Hinoki wood  
440 from Japanese historical buildings. *Comptes Rendus Phys* 10:601–611

441 Zhao J, Fu Z, Jia X, Cai Y (2016) Modeling conventional drying of wood: Inclusion of a  
442 moving evaporation interface. *Dry Technol* 34:530–538.  
443 <https://doi.org/10.1080/07373937.2015.1060999>

444 Zhou M, Caré S, Courtier-Murias D, et al (2018) Magnetic resonance imaging evidences of the  
445 impact of water sorption on hardwood capillary imbibition dynamics. *Wood Sci Technol*  
446 52:929–955. <https://doi.org/10.1007/s00226-018-1017-y>

447